RSC Advances

PAPER

View Article Online
View Journal | View Issue

Cite this: *RSC Adv.*, 2020, **10**, 38294

Syntheses, spectroscopic, redox, and structural properties of homoleptic Iron(III/II) dithione complexes†

Kyle J. Colston,[a] Sara A. Dille,[a] Benjamin Mogesa,[b] Jacilynn Brant,[c] Victor N. Nemykin,[d] Matthias Zeller[e] and Partha Basu *[a]

Received 27th August 2020
Accepted 10th October 2020

DOI: 10.1039/d0ra07371g

rsc.li/rsc-advances

Two sets of $Fe^{III/II}$ dithione complexes $[Fe^{II}(^{i}Pr_2Dt^0)_3][PF_6]_2$ ([**1**][PF_6]$_2$), $[Fe^{II}(Me_2Dt^0)_3][PF_6]_2$ ([**2**][PF_6]$_2$), and $[Fe^{III}(^{i}Pr_2Dt^0)_3][PF_6]_3$ ([**3**][PF_6]$_3$), $[Fe^{III}(Me_2Dt^0)_3][PF_6]_3$ ([**4**][PF_6]$_3$), and compound $[Fe^{III}(^{i}Pr_2Dt^0)_3][FeCl_4][PF]_2$ ([**3**][$FeCl_4$][PF_6]$_2$) were synthesized from *N*,*N*′-diisopropyl piperazine-2,3-dithione ($^{i}Pr_2Dt^0$) and *N*,*N*′-dimethyl piperazine-2,3-dithione (Me_2Dt^0) ligands. Complexes [**1**][PF_6]$_2$–[**4**][PF_6]$_3$ have been characterized by NMR, IR, and UV-visible spectroscopies, and by electrochemistry. The molecular structures of [**2**][PF_6]$_2$ and [**3**][$FeCl_4$][PF_6]$_2$ have been determined by X-ray crystallography. Complexes [**2**][PF_6]$_2$ and [**3**][$FeCl_4$][PF_6]$_2$ both crystallized in the monoclinic space group $P2_1/n$. Both complexes exhibit distorted octahedral geometry and the three coordinated ligands in each complex exhibit different dithione folding. Complexes [**1**][PF_6]$_2$–[**4**][PF_6]$_3$ exhibit a single $Fe^{III/II}$ based couple and three quasi-reversible ligand-based redox couples. The electronic spectra of [**1**][PF_6]$_2$–[**4**][PF_6]$_3$ show intense MLCT bands that indicate strong mixing between metal and ligand orbitals. DFT calculations were used to provide a framework for understanding the electronic origin of their redox chemistry and spectroscopic features.

Introduction

Transition metal complexes that possess dithiolene ligands, such as 1,2-ene-dithiolate (Dt^{2-}),[1] often exhibit strong metal–ligand interactions between the non-innocent ligand and metal ion which can result in a delocalized system.[2,3] Electron delocalization impacts the electronic structure of the complexes and can leave the redox state of the metal ion ambiguous.[4–7] Iron complexes containing reduced Dt^{2-} ligands have been of interest due to their electronic and structural properties.[1,8–24] A desired property for such materials includes the ability to absorb in the ultraviolet (UV), visible, or near infrared (NIR) spectral regions. The delocalized nature of the dithiolene-metal donor–acceptor system often shifts electronic transitions to lower energies. These transitions have also been shown to exhibit relatively high molar absorptivities.[25–28] Dithiolene ligands are redox active and can exist along two redox extremes; the reduced dianionic ene-1,2-dithiolate (Dt^{2-}) or oxidized neutral dithione (Dt^0).

Tris Dt^{2-} transition metal complexes were reported by several groups in the 1960s, including fundamental work by Holm,[29] Gray,[30] and others.[31,32] Only 5 such structures are Fe complexes; and all of which are of the general structure $[Fe(mnt)_3]^{2-/3-}$ (mnt = maleonitriledithiolate).[33] The structure of a putative Fe^{IV} complex, $[AsPh_4]_2[Fe(mnt)_3]$, was reported as early as in 1973,[34] and since then other Fe^{IV} and Fe^{III} complexes have been structurally examined.[35] $[Fe(mnt)_3]^{2-/3-}$ complexes are low spin due to the strong ligand field of mnt and exhibit a distorted octahedral geometry.[32,36] More recently, Milsmann *et al.* explored the electronic structure of both $[Fe(mnt)_3]^{2-}$ and $[Fe(mnt)_3]^{3-}$ complexes, demonstrating that the oxidation of Fe^{III} to Fe^{IV} was purely metal based.[35]

For a more complete understanding of Fe dithiolene chemistry; the properties of Fe complexes with fully oxidized Dt^0 ligands must be thoroughly characterized. The only reported tris chelate $[Fe(Dt^0)_3]^{2+}$ complex was recently described by Pilia *et al.* as a tetrafluroborate salt, $[Fe^{II}(Me_2Dt^0)_3][BF_4]_2$.[37] In this case, *N*,*N*′-dimethyl piperazine-2,3-dithione (Me_2Dt^0) supported a low-spin configuration. However, a homoleptic Fe^{III} DT^0 complex is yet to be reported. As a part of our ongoing efforts to understand the fundamental coordination chemistry of Dt^0 ligands, we have reported coordination chemistry of Zn,[38] Cu,[39] Ni[40] and Mo[41–44] complexes. Here we report the synthesis, structure and redox properties of homoleptic $[Fe^{II}(Dt^0)_3]^{2+}$ and

[a]Department of Chemistry and Chemical Biology, Indiana University-Purdue University, Indianapolis, IN, 46202, USA. E-mail: basup@iupui.edu

[b]Department of Chemistry and Biochemistry, Duquesne University, Pittsburgh PA, 15282, USA

[c]The Air Force Research Laboratory, Wright-Patterson AFB, OH, 45433, USA

[d]Department of Chemistry, University of Tennessee, Knoxville, TN, 37996, USA

[e]Department of Chemistry, Purdue University, West Layfette, IN, 47907, USA

† Electronic supplementary information (ESI) available. CCDC 1893657 and 1983658. For ESI and crystallographic data in CIF or other electronic format see DOI: 10.1039/d0ra07371g

$[Fe^{III}(Dt^0)_3]^{3+}$ complexes. With this current study we aim to explore and expand upon the fundamental understanding of Fe tris Dt^0 complexes with the characterization of the first ever reported $[Fe^{III}(Dt^0)_3]^{3+}$ complexes.

Materials and methods

Physical measurements

All syntheses were carried out in a dry box under an argon environment or under argon gas using Schlenk systems. Solvents were purified by distillation or using an LC Technological Solutions solvent purification system and were degassed before use. Anhydrous $FeCl_2$ and $FeCl_3$ were purchased from Sigma-Aldrich chemical company and used as received. *N*,*N*′-Dimethylpiperazine-2,3-dithione (Me_2Dt^0) and *N*,*N*′-diisopropyl piperazine-2,3-dithione ($^iPr_2Dt^0$) were synthesized according to literature procedures.[45] Electronic absorption spectra were recorded on a Shimadzu UV-3600 Plus spectrophotometer. ^{1}H NMR data was collected using either a Bruker Avance III 500 MHz spectrometer and spectra were referenced to residual protonated solvent. IR spectra were recorded on neat samples on a Thermo Electron 53 corporation Nicolet 380 spectrometer.

Cyclic voltammograms were recorded using a Metrohm Autolab PGSTAT204 potentiostat. A three-electrode cell system was employed with a Pt-disk working electrode, Pt-wire auxiliary electrode and Ag^+/Ag reference electrode in acetonitrile and tetrabutylammonium hexafluorophosphate was used as the supporting electrolyte. In all experiments, potentials were referenced *versus* Fc^+/Fc, which was added as an internal standard at the end of each measurement. Elemental analyses were performed, at the Midwest Microlab LLC, Indianapolis, IN. Conductivity measurements were carried out in 0.49 mM to 0.604 mM DMF solutions at 298 K using VWR Traceable conductivity probe.

Single crystal structure determinations

X-Ray quality single crystals of [**2**][PF_6]$_2$ and [**3**][$FeCl_4$][PF_6]$_2$ were obtained *via* slow diffusion of ether into acetonitrile solutions. Attempts to grow single crystals of [**3**][PF_6]$_3$ and [**4**][PF_6]$_3$ were unsuccessful. X-ray quality crystals were coated with paratone oil and mounted up on crystal micromounts, and data were collected using a Bruker SMART Apex II diffractometer. A graphite monochromator was used with Mo Kα radiation at 0.71073 Å. Absorption correction was performed using SADABS program,[46] and structure solution and refinement were done using SHELXS-97 (ref. 47) and SHEXLX-2018 programs,[48] using the graphical interface Shelxle.[49] Data were collected at either 296 K or 150 K (refinement details are included in the ESI†). Crystal and structure data for [**2**][PF_6]$_2$ and [**3**][$FeCl_4$][PF_6]$_2$ are given in Table 1. Complete crystallographic data, in CIF format, have been deposited (CCDC 1893657 and 1893658) with the Cambridge Crystallographic Data Centre. CCDC contains the supplementary crystallographic data for this paper.

Theoretical calculations

Computational studies for the **1** and **3** were performed using the Density Functional Theory (DFT) approach with Gaussian 09 running under UNIX OS.[50] Molecular orbital contributions were compiled from single point calculations using the QMForge program.[51] B3LYP and UB3LYP DFT methods were employed for closed and open-shell calculations, respectively.

Table 1 Crystal data for [**2**][PF_6]$_2$ and [**3**][$FeCl_4$][PF_6]$_2$

	[**2**][PF_6]$_2$	[**3**][PF_6]$_2$[$FeCl_4$]
Empirical formula	$C_{18}H_{30}F_{12}FeN_6P_2S_6$	$C_{30}H_{54}Cl_4F_{12}Fe_2N_6P_2S_6$
Formula weight	868.63	1234.59
Temperature/K	150K	296 K
Crystal system	Monoclinic	Monoclinic
Space group	$P2_1/n$	$P2_1/n$
a/Å	21.8709(8)	13.8301(4)
b/Å	6.3608(3)	27.0496(8)
c/Å	25.3626(9)	14.3517(5)
α/°	90.00	90.00
β/°	113.674(2)	102.910(2)
γ/°	90.00	90.00
Volume/Å^3	3231.4(2)	5233.2(3)
Z	4	4
Radiation type	Mo $K\alpha$	Mo $K\alpha$
μ/mm^{-1}	1.05	1.13
Crystal size/mm	0.17 × 0.16 × 0.07	0.26 × 0.24 × 0.01
Reflections collected	11 262	60 221
Independent reflections	11 262	9445
No. of parameters	456	808
No. of reflections	11 262	9445
Goodness-of-fit on F^2	1.08	1.02
Final R indexes	$R_1 = 0.053$, w$R_2 = 0.151$	$R_1 = 0.046$, w$R_2 = 0.133$

Wachter's full-electron basis set was used for all atoms in all calculations. Geometries were optimized starting from crystal structure coordinates, when available, without any symmetry restraints.

Magnetic measurements

Using a Quantum Design Physical Property Measurement System (PPMS) equipped with a Vibrating Sample Magnetometer (VSM), magnetization data were collected as a function of temperature (1.9 to 300 K) in applied fields of 0.1 T (1 kOe) and 0.5 T (5 kOe) for a 12.6 mg sample of $[Fe(Me_2Dt^0)_3][PF_6]_3$ that was packed in a cylindrical sample holder ($d = 2$ mm), yielding a sample height of $\approx$ 2.5 mm. Diamagnetic correction was applied as described in a recent review article by Sproules.[58]

$\chi_D = \chi_D(Fe^{3+}) + 18\chi_D(C) + 30\chi_D(H) + 6\chi_D$ (N, ring) $+ 6\chi_D$ (S) $+ 3\chi_D$ (P) $+ 18\chi_D$ (F) $= -10 + 18(-6.00) + 30(-2.93) + 6(-4.61) + 6(-15.0) + 3(-26.3) + 18(-6.3) = -515.86 \times 10^{-6}$ emu mol^{-1}.

Variable temperature NMR experiments were conducted using a Bruker AvanceIII 500 MHz NMR system utilizing a BVT3200 temperature control board and nitrogen evaporation system. Probe temperature was monitored with a standard Type T Thermocouple and temperature calibration was performed using deuterated methanol. Samples equilibrated for 10 minutes once the probe reached target temperatures.

Syntheses

Synthesis of $[Fe^{II}(^iPr_2Dt^0)_3][PF_6]_2$, ([1][PF$_6$]$_2$). In a Schlenk flask, anhydrous $FeCl_2$ (63 mg, 0.50 mmol) was dissolved in 10 mL of methanol and stirred for 10 min resulting in a clear solution. $^iPr_2Dt^0$ (380 mg, 1.65 mmol) was dissolved in 5 mL chloroform and added dropwise to the clear solution, resulting in a green reaction mixture. Neat sodium hexafluorophosphate (336 mg, 2.00 mmol) was added. The reaction mixture was stirred for 10 min after which a green precipitate was removed *via* filtration and dried under vacuum to obtain analytically pure material. Yield: 84% (435 mg, 0.42 mmol). Anal. calcd (experimental) for $C_{30}H_{54}F_{12}FeN_6P_2S_6$: C, 34.75 (34.25); H, 5.25 (5.26); N, 8.10(7.95); FTIR (neat, cm^{-1}): 1520 (*vs.*, C–N), 1312 (*vs.*, CN(S)), 1127, 1092, 816, 568 (*vs.*, PF_6); ^{1}H NMR (CD_3CN): δ, ppm = 5.36 (m, 6H, CH), 3.73 (s, 12H, CH_2), 1.35 (d, 36H, CH_3); UV-Vis (acetonitrile): λ_{max} (ε, M^{-1} cm^{-1}) = 923(4040); 805(3960); 593 (sh, 7500); 362 (sh, 15 510); 305 (19 410); 218(33 550); conductivity: Λ_M (Ω^{-1} cm^2 mol^{-1}): 235.

Synthesis of $[Fe^{II}(Me_2Dt^0)_3][PF_6]_2$, ([2][PF$_6$]$_2$). Into a dry Schlenk flask, anhydrous $FeCl_2$ (36 mg, 0.50 mmol) was dissolved in 10 mL of methanol. Into the reaction mixture, Me_2Dt^0 (289 mg, 1.65 mmol) ligand in 10 mL of chloroform was added at room temperature. The reaction mixture turned green almost instantaneously upon addition of the ligand. The mixture was then stirred for another 10 min, after which the product precipitated upon addition of excess sodium hexafluorophosphate (336 mg, 2.00 mmol). The product was isolated by filtration and washed with chloroform (3 × 1 mL) to obtain analytically pure material. Yield: 87% (376 mg, 0.43 mmol). Calcd (experimental) for $C_{18}H_{32}F_{12}Fe_1N_6P_2S_6$: C, 24.89 (24.33); H, 3.48 (3.25); N, 9.67 (9.33); FTIR (neat, cm^{-1}): 1520 (*vs.*, C–N), 1364 (*vs.*, CN(S)), 1156, 1099, 837, 555 (*vs.*, PF_6); ^{1}H NMR (CD_3CN): δ, ppm = 3.82 (s, 12H, CH_2), 3.56 (s, 18H, CH_3); UV-Vis (acetonitrile): λ_{max} (ε, M^{-1} cm^{-1}) = 887 (3380); 779 (3280); 349 (13 310); 292 (23 270); 216 (37 050).

Synthesis of $[Fe(^iPr_2Dt^0)_3][PF_6]_3$, ([3][PF$_6$]$_3$). Into a Schlenk flask under argon, anhydrous $FeCl_3$ (60 mg, 0.38 mmol) was dissolved in 10 mL of methanol. Into this solution three equivalents of $^iPr_2Dt^0$ (285 mg, 1.24 mmol) was added, in 10 mL of methanol, yielding a dark green solution. The product was precipitated by addition of sodium hexafluorophosphate (310 mg, 1.85 mmol). The final product was collected by filtration and washed with cold chloroform (2 × 1 mL) to obtain analytically pure material. Yield 85% (317 mg 0.27 mmol) calcd (experimental) for $C_{30}H_{54}F_{18}FeN_6P_2S_6$: C, 30.49 (30.11); H, 4.61 (4.20); N, 7.11 (7.00); FTIR (neat, cm^{-1}): 1520 (*vs.*, C–N), 1356 (*vs.*, CN(S)), 1115, 1095, 833, 551 (*vs.*, PF_6). ^{1}H NMR (CD_3CN): δ, ppm = 26.70 (br, 2H, CH_2), 24.17 (br, 2H, CH_2), 6.15 (br, 1H, CH_2), 5.60 (br, 1H, CH_2), 5.34 (br, 2H, CH_2), 4.83 (br, 2H, CH_2), 3.72 (br, 2H, CH_2), 2.74 (br, 6H, CH), 1.34 (br, 12H, CH_3), 0.45 (br, 6H, CH_3); UV-Vis (acetonitrile): λ_{max}(ε, M^{-1} cm^{-1}) = 657 (sh, 3790); 537 (sh, 4920); 353 (27 620); 292 (29 010); 228 (33 530); conductivity: Λ_M (Ω^{-1} cm^2 mol^{-1}): 354.

Synthesis of $[Fe(Me_2Dt^0)_3][PF_6]_3$, ([4][PF$_6$]$_3$). Into a Schlenk flask under argon, anhydrous $FeCl_3$ (81 mg, 0.50 mmol) was dissolved in 10 mL of THF. Into this solution were added three equivalents of Me_2Dt^0 (290 mg, 1.53 mmol) dissolved in 2 mL of chloroform, yielding a dark green solution. The product was precipitated by addition of sodium hexafluorophosphate (420 mg, 2.50 mmol). The final product was collected by filtration and washed with cold chloroform (2 × 1 mL) to obtain analytically pure material. Yield 70% (370 mg, 0.35 mmol) calcd (experimental) for $C_{18}H_{30}F_{18}FeN_6P_2S_6$ + MeOH: C, 21.83 (22.37); H, 3.28 (3.06); N, 8.04 (8.64); FTIR (neat, cm^{-1}): 1520 (*vs.*, C–N), 1348 (*vs.*, CN(S)), 1132, 1099, 829, 555 (PF_6).; ^{1}H NMR (CD_3CN), δ, ppm = 30.29 (br, 1H, CH_2), 24.55 (br, 1H, CH_2), 17.80 (br, 2H, CH_2), 6.09 (br, 2H, CH_2), 5.49 (br, 2H, CH_2), 3.79 (br, 9H, CH_3), 3.56 (br, 9H, CH_3), −0.33 (br, 4H, CH_2); UV-Vis (acetonitrile): λ_{max} (ε, M^{-1} cm^{-1}) = 882 (4550); 529 (3470); 342 (28 900); 281(35 460) 215 (44 030); conductivity: Λ_M (Ω^{-1} cm^2 mol^{-1}): 376.

Synthesis of $[Fe(^iPr_2Dt^0)_3][FeCl_4][PF_6]_2$, ([3][FeCl$_4$][PF$_6$]$_2$). Into a Schlenk flask under argon, anhydrous $FeCl_3$ (50 mg, 0.31 mmol) was stirred in 5 mL of MeOH until dissolved. Into the yellow solution, solid $^iPr_2Dt^0$ (142 mg, 0.63 mmol) was added to produce a dark green solution. The reaction mixture was stirred for 30 minutes. The product was then precipitated from solution by the addition of two equivalents of sodium hexafluorophosphate (90 mg, 0.63 mmol) to afford a dark green solid. The solid was washed with cold chloroform (2 × 1 mL) to remove excess ligand. The solid was then dissolved in acetonitrile and filtered with a Millipore. The acetonitrile was then removed under reduced pressure to afford a dark green solid. Yield 26% (100 mg, 0.08 mmol) calcd (experimental) for $C_{30}H_{54}F_{12}Fe_2N_6P_2S_6$ + CH_3CN: C, 30.13 (30.69), H, 4.50 (4.39), N, 7.69 (7.15).

Results and discussion

Magnetic properties

Complexes [**1**][PF_6]$_2$ and [**2**][PF_6]$_2$ are diamagnetic as evidenced from their ^{1}H NMR spectra and exhibit chemical shifts consistent with their respective coordinated Dt^0 ligand, albeit their resonances appear upfield from those observed for free Dt^0 ligand. This is consistent with Pilia *et al.*'s finding.[37] The ^{1}H NMR spectrum of [**4**][PF_6]$_3$ exhibit paramagnetically shifted resonances outside the normal diamagnetic envelope as shown in Fig. S1.†[52–54] The resonances for the methylene CH_2 protons (12H) are observed as six broad peaks which indicates significant delocalization of the spin density for the unpaired electron. The resonances observed at 30.29 ppm, 24.55 ppm, and 17.80 ppm integrate to a total of ~4H, which suggests that one of Dt^0 ligands has a significantly different spin density when compared to the other two ligands. Similar results are observed for [**3**][PF_6]$_3$ shown Fig. S2.†

The paramagnetic chemical shift (δ_{para}) has two contributions – isotropic (δ_{iso}) and diamagnetic (δ_{dia}). Considering the similar geometries of Fe^{II} and Fe^{III} complexes, the difference between their resonances can be used to calculate the δ_{iso} contribution (eqn (1)). δ_{iso} shifts for [**3**][PF_6]$_3$ and [**4**][PF_6]$_3$ exhibit Curie behavior (Fig. 1) as a function of temperature. The amount of spin density on a nucleus positively correlates with the δ_{iso} resonance observed in the ^{1}H NMR spectrum. The δ_{iso} shift originates from dipole–dipole interactions between nuclear and electron magnetic moments, dipolar contribution ($\delta_{dipolar}$), and Fermi contact interactions that result from unpaired electron spin density delocalizing on the ligand, contact contribution ($\delta_{contact}$) (eqn (2)).[55] Therefore, CH_2 protons that are closer to delocalized spin density will have larger $\delta_{contact}$ shifts and produce resonances further downfield. The proximity of the CH_2 proton to the Fe center can also be observed due to distance-dependent signal broadening. Fe can act as a relaxing agent through dipolar interactions, observed as increased line width, dependent on the distance between nuclei ($\propto r^{-6}$).[56] Using the H···Fe distances from the calculated optimized structure of [**4**][PF_6]$_2$ and the full width at half maxima (Hz) the three most downfield resonances are assigned in Fig. S1.†

$$\delta_{iso} = \delta_{para} - \delta_{dia} \quad (1)$$

$$\delta_{iso} = \delta_{dipolar} + \delta_{contact} \quad (2)$$

The solid-state magnetic behavior of complex [**4**][PF_6]$_3$ was studied as a function of temperature using a vibrating sample magnetometer (VSM). The data collected between 1.9 and 300 K in applied fields of 0.1 T (1 kOe) and 0.5 T (5 kOe) show a molar magnetic susceptibility consistent with $s = 1/2$ ground state (Fig. S3†). The Curie–Weiss fit of the magnetization data at H = 1 kOe was used to calculate the effective magnetic moment $\mu_{Fe} = 1.8\ \mu_B$. This observation corresponds well with the observed temperature dependence for the resonances of the paramagnetic shifts observed in the ^{1}H NMR spectrum of [**4**][PF_6]$_3$.

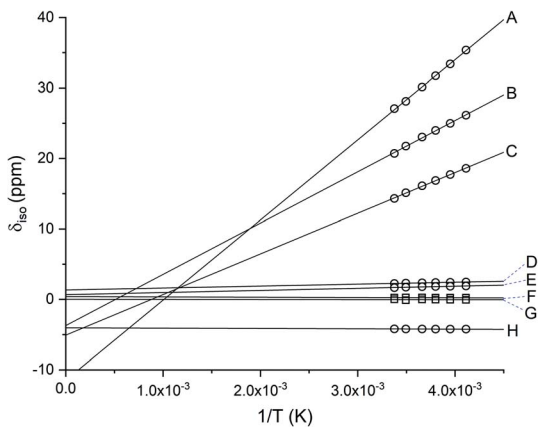

Fig. 1 Linear fit of the isotropic shift for [**4**][PF_6]$_3$ as a function of inverse temperature. Methylene CH_2 protons are represented as ○ and methyl CH_3 protons are represented as □. The signals for CH_2 protons suggest significant delocalization of the spin density, δ_{para} for both [**3**][PF_6]$_3$ and [**4**][PF_6]$_3$. Resonances for all protons (A–H) in variable temperatures are provided in Table S1.†

Molecular structures

The thermal ellipsoid plots of [**2**][PF_6]$_2$ and [**3**][$FeCl_4$][PF_6]$_2$ are shown in Fig. 2 and selected bond lengths and angles are listed in Table 2. Both complexes [**2**][PF_6]$_2$ and [**3**][$FeCl_4$][PF_6]$_2$ crystallize in the monoclinic crystal system and in the $P2_1/n$ space group. The first coordination sphere of the metal center consists of three bidentate Dt^0 ligands coordinating through the sulfur atoms. The average ligand bite angle of [**2**][PF_6]$_2$ and [**3**][$FeCl_4$][PF_6]$_2$ are 87° and 89°, respectively. Ligand bite angles of ~90° indicate minimal distortion from an ideal octahedral geometry. Previously reported iron dithiolene complexes [$Fe(Me_2Dt^0)_3$][BF_4]$_2$ (ref. 37) and $[Fe^{III/IV}(mnt)_3]^{n-}$, (where mnt^{2-} = maleonitrile dithiolate; $n = 3, 2$)[34,35,57,58] also exhibit distorted octahedral geometry in their crystal structures. [**2**][PF_6]$_2$ and [**3**][$FeCl_4$][PF_6]$_2$ exhibit similar packing motifs to that of [$Fe(Me_2Dt^0)_3$][BF_4]$_2$ with short contacts observed between the anions and carbon atoms of the Dt^0 ligands.[37]

Given the redox active nature of the dithiolene ligand, establishing the oxidation state of the ligands after coordination to a metal center is important. The average Fe–S distances for [**2**][PF_6]$_2$ and [**3**][$FeCl_4$][PF_6]$_2$ are 2.253(10) Å and 2.258(11) Å, respectively, and the average Fe–S distances for $[Fe^{IV/III}(mnt)_3]^{2-/3-}$ complexes ranges between 2.263 and 2.287 Å. The average Fe–S distance in the only structurally characterized iron Dt^0 complex, [$Fe(Me_2Dt^0)_3$][BF_4]$_2$ is 2.294(13) Å.[37] This indicates that the Fe–S bond lengths are poor reporters of ligand and metal oxidation state.

The C–S and C–C bond lengths of the dithiolene moiety can change depending on the number of π electrons present[59] and thus be used to determine the oxidation state of Dt^0 in metallodithiolene complexes. The average C–S bond lengths of [**2**][PF_6]$_2$ and [**3**][$FeCl_4$][PF_6]$_2$ are 1.685(3) Å and 1.686(4) Å, and the average C–C bond length for the dithiolene moiety are 1.481(6) Å and 1.50(5) Å, respectively. These bond lengths support that the ligands are fully oxidized and match well with the Dt^0 bonds reported for [$Fe(Me_2Dt^0)_3$][BF_4]$_2$.[37] In comparison, the average

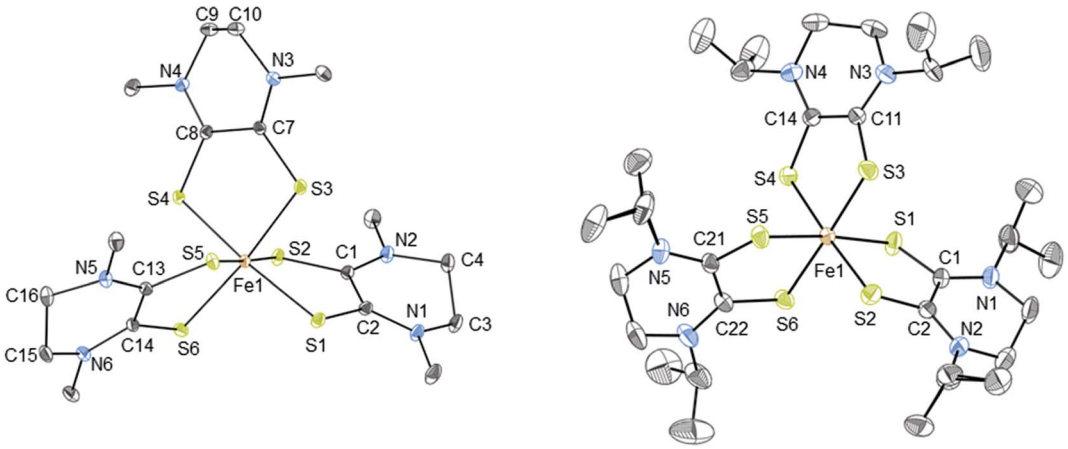

Fig. 2 Thermal ellipsoid plots (30%) of complex **2** (left) and **3** (right). Hydrogen atoms were omitted and only one conformation of the ^{i}Pr substituents are shown for clarity. Refinement details of the ^{i}Pr groups are described fully in the ESI.†

Table 2 Selected bond lengths (Å) and angles (°) for [**2**][PF_6]$_2$ and [**3**][$FeCl_4$][PF_6]$_2$

[**2**][PF_6]$_2$				[**3**][$FeCl_4$][PF_6]$_2$			
Fe1–S1	2.2355 (9)	C1–C2	1.484 (5)	Fe1–S1	2.2565(11)	C24–C23	1.491 (7)
Fe1–S2	2.2612 (10)	C7–C8	1.479 (4)	Fe1–S2	2.2610 (11)	S1–Fe1–S2	87.90 (4)
Fe–S3	2.2553 (9)	C13–C14	1.481 (5)	Fe1–S3	2.2604(10)	S1–Fe1–S3	92.84 (4)
Fe–S4	2.2614 (9)	C3–C4	1.500 (6)	Fe1–S4	2.2484(10)	S4–Fe1–S1	89.74 (4)
Fe1–S5	2.2453 (9)	C9–C10	1.489 (6)	Fe1–S5	2.2608 (11)	S1–Fe1–S5	174.58 (4)
Fe1–S6	2.2642 (10)	C15–C16	1.511 (5)	Fe1–S6	2.2666 (11)	S1–Fe1–S6	87.52 (4)
S1–C1	1.683 (3)	S1–Fe1–S5	96.24 (3)	S1–C1	1.682 (3)	S3–Fe1–S2	88.52 (4)
S2–C2	1.689 (3)	S1–Fe1–S3	87.78 (3)	S2–C2	1.684 (4)	S4–Fe1–S2	176.78 (4)
S3–C7	1.680 (3)	S5–Fe1–S3	172.52 (4)	S3–C11	1.698 (4)	S5–Fe1–S2	89.20 (4)
S4–C8	1.684 (3)	S1–Fe1–S2	87.22 (3)	S4–C12	1.689 (3)	S2–Fe1–S6	94.08 (4)
S5–C13	1.694 (3)	S5–Fe1–S2	93.89 (4)	S5–C21	1.694(4)	S4–Fe1–S3	89.41 (4)
S6–C14	1.680 (3)	S3–Fe1–S2	92.60 (4)	S6–C22	1.675 (4)	S5–Fe1–S3	91.65 (4)
S3–Fe1–S4	87.95 (3)	S1–Fe1–S4	171.78 (4)	C1–C2	1.493 (5)	S3–Fe1–S6	177.38 (4)
S2–Fe1–S4	85.96 (4)	S5–Fe1–S4	88.80 (3)	C11–C12	1.499 (5)	S4–Fe1–S5	93.33 (4)
S1–Fe1–S6	94.62 (4)	S5–Fe1–S6	87.27 (3)	C21–C22	1.503 (5)	S4–Fe1–S6	88.00 (4)
S2–Fe1–S6	177.71 (4)	S3–Fe1–S6	86.12 (3)	C4–C3	1.490 (6)	S5–Fe1–S6	88.13 (4)
		S4–Fe1–S6	92.09 (4)	C14–C13	1.494 (6)		

bond C–C bond lengths of $[Fe(mnt)_3]^{n-}$ complexes are 1.353 Å for Fe^{II} complexes[34,35,57] and 1.368 Å for Fe^{III}.[35,58] The shorter C–C bond lengths of the mnt dithiolene moieties indicate reduced Dt^{2-} ligands.

Table 3 compares Fe–X (X is ligand donor atom) bond lengths, average ligand bite, and distortion (Θ_{avg}) of the C_3 axis for [**2**][PF_6]$_2$ and [**3**][$FeCl_4$][PF_6]$_2$ with relevant Fe^{III} tris complexes; $[Fe^{III}(mnt)_3]^{3-}$, $[Fe^{III}(cat)_3]^{3-}\cdot 1.5H_2O$ (cat = catecholato),[60] Fe^{III}(3,6-DBSQ)$_3$ (3,6-DBSQ = 3,6-di-*tert*-butyl-1,2-benzoquinone),[61] and Fe^{III}(3,5-DBSQ)$_3$ (3,5-DBSQ = 3,6-di-*tert*-butyl-1,2-benzoquinone).[62] These complexes were chosen as representatives for the redox extremes of reduced dithiolene or

Table 3 Comparison of selected Fe–X (X = S, O) bond lengths (Å) and average bite (°) and distortion (Θ_{avg}) along the three-fold axis in [**2**][PF_6]$_2$ and [**3**][$FeCl_4$][PF_6]$_2$ of this work with relevant Fe^{III} complexes

Complex	Bite angle	Θ_{avg}	Fe–X^1	Fe–X^2	Fe–X^3	Ref.
[**2**][PF_6]$_2$	87.48	54.83	2.245, 2.264	2.235, 2.261	2.256, 2.261	This Work
[**3**][$FeCl_4$][PF_6]$_2$	88.48	55.48	2.259, 2.267	2.262, 2.249	2.260, 2.257	This Work
$[Fe^{III}(mnt)_3]^{3-}$	89.00	53.35	2.257, 2.261	2.257, 2.261	2.271, 2.271	35
$[Fe^{III}(cat)_3]^{3-}\cdot 1.5H_2O$	81.26	44.52	2.016, 2.018	1.999, 2.025	1.995, 2.035	60
Fe^{III}(3,6-DBSQ)$_3$	78.42	43.39	1.973, 1.992	2.016, 2.020	1.998, 2.011	61
Fe^{III}(3,5-DBSQ)$_3$	78.69	38.97	2.022, 2.012	2.003, 2.029	2.014, 2.011	62
$[Fe^{II}(Me_2pipto)_3]^{2+}$	78.56	42.22	2.485, 2.071	2.485, 2.071	2.510, 2.041	63

catechol and a single electron oxidized semiquinone Fe^{III} complexes. Additionally, an octahedral Fe^{II} complex containing sulfur–oxygen mixed donor ligands, $[Fe^{II}(Me_2pipto)_3]^{2-}$ (Me_2-pipto = *N*,*N*′-dimethyl-piperazine-3-oxo-2-thione),[63] is included to allow for comparison to a system with both donor atoms. Sulfur-based ligands displayed average bite angles of 87.48° to 89.00° while oxygen-based ligands showed significantly smaller bite angles ranging from 78.42° to 81.26°, respectively. Distortion (Θ_{avg}) angles were measured for each ligand *via* a projection down the C_3 axis of the primary coordination sphere and averaged, illustrated in Fig. 3. Such distortion is directly related to a mechanism for racemization of octahedral complexes with three bidentate ligands known as the trigonal twist. An angle of $\Theta = 60°$ corresponds to O_h symmetry while $\Theta = 0°$ corresponds to D_{3h} symmetry. Twist distortion and ligand bite angle are the result of differences in ligand field splitting brought by ligand coordination, and such distortions are well documented for Fe tris dithiolene complexes.[64]

The Θ_{avg} of sulfur-based ligands range from 53.35° to 54.83° and is ~12° greater than what is observed for complexes with oxygen-based ligands. The bite angles and Θ_{avg} for the sulfur–oxygen mixed donor system are also like those reported for semiquinone complexes. The lesser distortion observed for Fe tris dithiolene complexes is indicative of a larger ligand-field stabilization energy. The greater distortion observed for semiquinone and catecholate Fe^{III} complexes corresponds to higher energy e′ orbitals which results in a ground state of unevenly filled degenerate orbitals *vide infra*.

Comparing complexes with reduced ligands to their oxidized counterparts, it is apparent that the reduction of Dt^0 ligands has less of an impact on molecular distortion. The two-electron oxidation of the dithiolene moiety increases Θ_{avg} by 1.3°, whereas the single electron oxidation to the semiquinone ligand decreases Θ_{avg} by 2.2°. The differences in bond lengths and the distortion between ligands of the same compound are a result of a pseudo Jahn–Teller effect present from nearly degenerate electronic states.

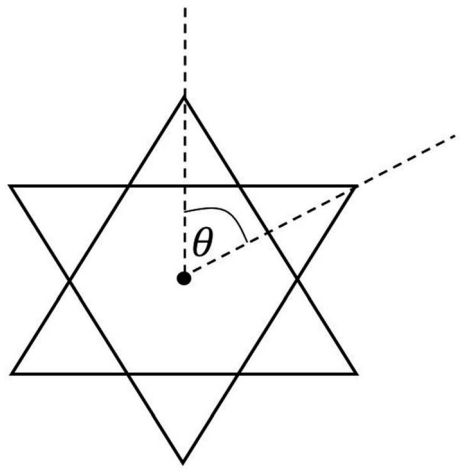

Fig. 3 Illustration of distortion with Θ with a projection along the C_3 axis of a compound with Oh symmetry.

Electrochemistry

The electrochemical properties of the Fe^{II} and Fe^{III} complexes were investigated by cyclic voltammetry in acetonitrile solutions. The redox potentials are given in Table 4 and representative cyclic voltammograms for $[\mathbf{3}][PF_6]_3$ are presented in Fig. 4. The electrochemical responses of $[Fe(Dt^{2-})_3]^{2-}$ complexes typically exhibit a single metal based couple, and electrochemical properties are more dependent upon the metal center than the nature of the dithiolene ligand.[58] All complexes exhibit a single $Fe^{III/II}$ based couple at ~140 mV, however, the redox potential is influenced by the Dt^0 substituent, Fig. S4.† The observed $E_{1/2}$ of $^iPr_2Dt^0$ containing complexes were less positive than corresponding complexes with the Me_2Dt^0 ligand, and there were 77 mV and 66 mV differences in the redox couple for the Fe^{II} and Fe^{III} complexes, respectively.

It has been reported that the Dt^0 ligands in $[M(Me_2Dt^0)_2]^{2+}$ (M = Ni, Pt, Pd)[65] and $[Ni(^iPr_2Dt^0)_2]^{2+}$ (ref. 40) can participate in redox processes. The redox couples of $[M(R_2Dt^0)_2]^{2+}$ complexes are well resolved, and four distinct couples are observed. Electronically asymmetric square planar Ni complex containing both Dt^0 and Dt^{2-} ligands exhibit two reversible redox couples corresponding to the reduction of Dt^0.[66] Theoretically, electrochemical perturbation of a tris Dt^0 complex should result in six reversible ligand-based redox couples, however, only three couples between −1000 mV and −2100 mV are observed. The presence of three couples could be the result poor resolution, as redox potentials for multiple couples coincide with one another, or couples lie outside the electrochemical widow of the solvent. Attempts to resolve peaks utilizing various scan rates and differential pulse voltammetry (DPV) (Fig. S5 and S6†) were

Table 4 Redox potentials in mV of complexes $[\mathbf{1}][PF_6]_2$–$[\mathbf{4}][PF_6]_3$ in acetonitrile solutions containing $[Bu_4N][PF_6]$ using a scan rate of 100 mV/s^{-1} and a Pt disk, Pt wire, and Ag^+/Ag electrodes. Potentials are referenced to Fc^+/Fc couple

Complex	$E^1_{1/2}$ (ΔE_p)	$E^2_{1/2}$ (ΔE_p)	$E^3_{1/2}$ (ΔE_p)	$Fe^{III/II}$ $E_{1/2}$ (ΔE_p)
$[\mathbf{1}][PF_6]_2$	−1120 (130)	−1600 (290)	−2036 (320)	111 (130)
$[\mathbf{2}][PF_6]_2$	−1075 (195)	−1554 (302)	−2002 (397)	188 (133)
$[\mathbf{3}][PF_6]_3$	−1142 (152)	−1479 (189)	−1970 (263)	102 (114)
$[\mathbf{4}][PF_6]_3$	−1133 (81)	−1490 (162)	−1991 (185)	168 (110)

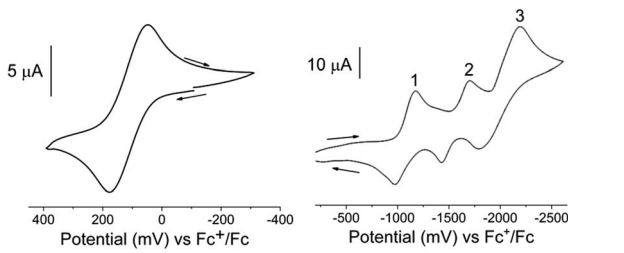

Fig. 4 Cyclic voltammograms of the $Fe^{III/II}$ (left) and ligand-based (right) redox couples of $[\mathbf{3}][PF_6]_3$ in an acetonitrile solution containing $[Bu_4N][PF_6]$. Recorded using a scan rate of 100 mV s^{-1} and a Pt disk working, Pt wire counter, and Ag^+/Ag reference electrodes. Additional voltammograms are shown in ESI Fig. S5 and S6.†

unsuccessful. Although the ligand-based couples are not well-resolved, the effect of the ligand substituents can still be observed. The $E_{1/2}$ for the three ligand-based couples are ~27 mV, ~18 mV, and ~19 mV more negative, respectively, for complexes that contain $^{i}Pr_2Dt^0$ ligands. The ^{i}Pr substituent is a better electron donating group which makes adding an electron to the system more difficult. Similar differences in ligand-based redox potential based on Dt^0 substituent have been reported on square planar d^8 metal complexes.[67]

Electronic absorption spectra

Electronic absorption spectra of all complexes were recorded in acetonitrile solutions and are shown in Fig. 5. [**1**][PF_6]$_2$ and [**2**][PF_6]$_2$, exhibit a broad band between 750 and 1200 nm (13 333–8333 cm^{-1}), which is proposed to be a metal-to-ligand charge transfer (MLCT) transition. Similar low energy bands have been observed for Fe^{II} complexes of coordinated carbonyls, dithiooxamide ligands,[68] and dithiolene ligands.[36]. $[Fe^{IV}(mnt)_3]^{2-}$ exhibits a similar low energy band at 806 nm (12 406 cm^{-1}) similar to complexes [**1**][PF_6]$_2$ and [**2**][PF_6]$_2$.[36] Absorption spectra observed for both [**2**][PF_6]$_2$ and [$Fe(Me_2Dt^0)_3$][BF_4]$_2$ are similar.[37] TD-DFT calculations support charge transfer band assignment for **1** as detailed in Fig. S7 and Table S2.†

Fe^{III} complexes [**3**][PF_6]$_3$ and [**4**][PF_6]$_3$ exhibit a broad shoulder between 590 nm and 800 nm (16 949–12 500 cm^{-1}) and [**4**][PF_6]$_3$ also exhibits a broad band between 800 nm and 1000 nm (12 500–10 000 cm^{-1}). Unlike $[Fe(mnt)_3]^{3-}$, which exhibits absorbance bands between 714 nm and 990 nm (14 005–10 100 cm^{-1}),[36] there is no transition observed below 650 nm (15 380 cm^{-1}) for [**3**][PF_6]$_3$, however complex [**4**][PF_6]$_3$ exhibits a broad band around 880 nm (11 360 cm^{-1}). While the molar absorptivity is greater than that expected of a d–d transition (Table S3†), the higher molar absorptivity in these complexes could be due to the mixing between the ligand and the metal orbitals. Attempts to model excited state transitions for **3** with TD-DFT calculations were unsatisfactory as open-shell systems remain a challenge for such calculations.

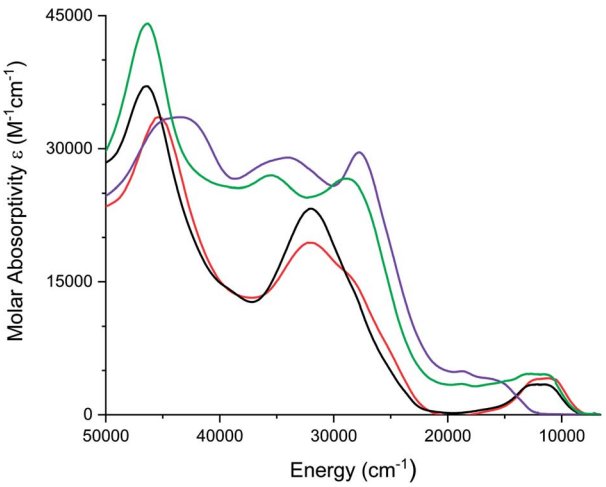

Fig. 5 Electronic spectra of [**1**][PF_6]$_2$ (red), [**2**][PF_6]$_2$ (black), [**3**][PF_6]$_3$ (purple), and [**4**][PF_6]$_3$ (green) recorded in acetonitrile.

Electronic structure

The electronic structures of the cationic complexes were investigated using density functional theory calculations. For **1**, calculations were conducted in the spin restricted mode with an $s = 0$ spin state. The initial geometry for **1** was obtained by replacing methyl substituents with isopropyl substituents on the ligands of the crystal structure for [**2**][PF_6]$_2$. The frontier orbitals and energy diagram are shown in Fig. 6 and the orbital compositions are listed in Table 5. For **3**, the crystal structure of [**3**][$FeCl_4$][PF_6]$_2$ was used as the initial structure and the calculation was conducted in a spin unrestricted mode for a $s = 1/2$ ground state. The frontier orbitals and energy diagrams are shown in Fig. S8† and the orbital compositions are listed in Table 5.

DFT calculations were performed on potential spin states for **1** and **3**. The optimization energies show the preferred low spin configuration for both complexes (Table S4†) which is consistent with physical measurement data. DFT optimized coordinates for **1** and **3** are given in Tables S5 and S6.† Here we only discuss the low-spin configuration, as the magnetic measurements support a $s = 1/2$ ground state. The atomic orbital contributions to the frontier molecular orbitals along with the energies are listed in Table 5. The HOMO of Fe^{II} complex **1** is mainly a Fe based (~55%) and the electron density of the HOMO-1 is shared between the three Dt^0 ligands. The LUMO is mainly based on a single Dt^0 ligand (~16% on the sulfur atoms and 49% on the piperazine ring) and the electron density of the LUMO−1 is shared between the remaining two Dt^0 ligands. The near degeneracy of the HOMO/HOMO−1 orbitals for **1** and α-set of **3** support the pseudo Jahn–Teller distortion observed in the crystal structures for [**2**][PF_6]$_2$ and [**3**][$FeCl_4$][PF_6]$_2$.

The spin density plot for the unpaired electron of **3**, presented Fig. 7, indicates spin density delocalized on the Dt^0 ligands. This contrasts from previously reported $[Fe^{III}(mnt)_3]^{3-}$

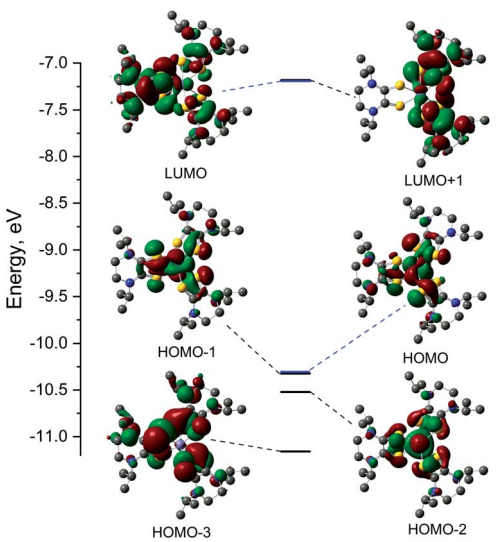

Fig. 6 Frontier orbitals and energy diagrams of **1**. Energies are relative and each molecular orbital is paired with its corresponding energy on the diagram. HOMO and LUMO are highlighted blue for clarity.

Table 5 Percent atomic orbital contributions of the frontier molecular orbitals for **1** and **3**; S represents the contribution of the sulfur atoms while L represents the contribution from all atoms of the $^{i}Pr_2Dt^0$ ligand. Superscripts 1, 2, and 3 identifies each ligand

Orbital	*E*, eV	Fe (d)	S^1	L^1	S^2	L^2	S^3	L^3
$[Fe^{II}(^{i}Pr_2Dt^0)_3]^{2+}$ (1)								
L + 1	−7.179	2.65	11.73	48.79	11.45	47.53	0.54	1.01
LUMO	−7.182	2.65	3.95	15.61	4.30	17.09	15.50	64.64
HOMO	−10.322	54.46 (d_{xy})	10.91	16.58	7.80	15.37	3.19	13.51
H − 1	−10.323	54.50 (d_{yz})	3.69	13.69	6.79	14.95	11.40	16.79
H − 2	−10.521	45.44 (d_{xz})	5.38	16.59	5.40	16.64	5.38	16.60
H − 3	−11.159	0.21	23.34	37.99	17.73	23.10	24.90	38.32
$[Fe^{III}(^{i}Pr_2Dt^0)_3]^{3+}$ (3) α spin set								
L + 1	−10.590	5.58	8.00	26.53	9.36	29.40	11.45	38.39
LUMO	−10.617	2.41	17.66	66.57	1.87	4.78	7.01	25.98
HOMO	−14.202	22.64 (d_{xy})	8.95	10.61	9.13	14.82	28.20	51.55
H − 1	−14.226	2.63 (d_{xy})	5.57	7.92	38.83	62.00	18.38	27.35
H − 2	−14.313	7.47 (d_{yz})	31.46	51.26	15.13	27.45	8.42	13.59
H − 3	−14.374	11.50 (d_{xz})	34.08	52.99	9.19	14.02	11.49	21.15
$[Fe^{III}(^{i}Pr_2Dt^0)_3]^{3+}$ (3) β spin set								
L + 1	−10.498	2.01	4.27	9.98	4.13	14.85	20.30	73.05
LUMO	−10.933	17.74 (d_{xy})	5.93	42.79	4.32	18.49	5.09	20.91
HOMO	−13.863	38.52 (d_{yz})	11.80	17.61	11.38	20.99	11.03	22.36
H − 1	−14.076	31.42 (d_{xz})	21.41	34.41	7.28	17.74	6.22	15.62
H − 2	−14.236	0.06	7.26	11.83	31.62	48.49	25.06	39.56
H − 3	−14.334	0.76	22.56	41.00	14.70	23.13	20.00	34.84

in which the spin density is shown to reside on Fe.[35] The electron deficient nature of the Dt^0 ligand facilitates spin delocalization across the metal-Dt^0 moiety. In contrast, the reduced nature of the mnt ligand does not produce the same spin delocalization, and the spin density of $[Fe(mnt)_3]^{2-/3-}$ complexes remains more localized on Fe. Delocalized spin density across the metal–dithiolene moiety is indicative of strong metal–ligand orbital mixing which contributes to the intense low energy bands observed in the electronic spectra for these complexes. The low energy transitions observed in the electronic spectra for **1** are assigned as MLCT. The highest energy donator orbitals for both complexes are predominantly metal-based, whereas the lowest lying acceptor orbital for both complexes are redox-active π* Dt^0 orbitals (HOMO → LUMO). Higher energy transitions are assigned to be ILCT bands between Dt^0 π and orthogonal π* orbitals of the Dt^0 ring (HOMO−3 → LUMO). The asymmetric nature of the spin delocalization indicates that Dt^0 ligands are electronically asymmetric and can act independently from one another in CT processes.

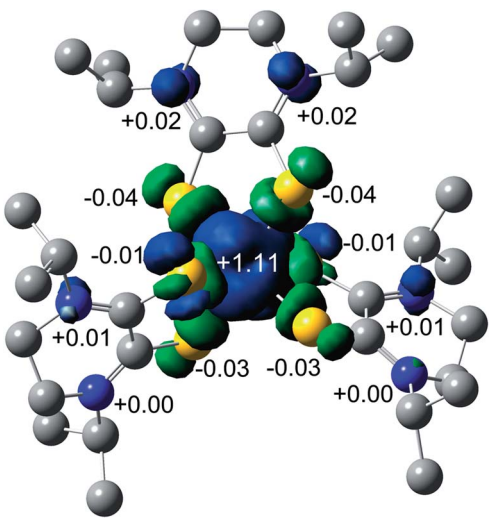

Fig. 7 Mulliken spin density plot for **3**.

Conclusions

This manuscript reports the syntheses and characterization of tris Dt^0 complexes of both Fe^{II} and Fe^{III}. redox states. Crystal structures indicate that there was little difference in structure between the two metal oxidation states. Both Fe^{II} and Fe^{III} complexes are low-spin. Variable temperature and variable field magnetic moments indicate that Fe^{III} has a ground spin state of $s = 1/2$ which is consistent with the observed paramagnetically shifted NMR spectra. The magnetic moment and the Fe^{II} complexes exhibit low energy bands that have been assigned to be metal-to ligand charge transfer in origin. The molar absorptivity is consistent with ligand–metal orbital mixing as supported by DFT calculations. The electrochemical behavior implies extensive ligand-based reduction. In addition to the ligand based redox couples, one metal-based couple was observed. The results indicate that efficient mixing of metal–ligand orbitals is not dependent on the oxidation state of the ligand. Such efficient mixing increases the ligand field resulting in low spin complexes. Further studies are needed to fully

understand the magnetic behavior and whether NMR spectroscopy can serve to quantitatively describe the $\delta_{contact}$ and $\delta_{dipolar}$ contributions related to electron delocalization.

Conflicts of interest

There are no conflicts to declare.

Acknowledgements

Financial support from the School of Science, IUPUI is gratefully acknowledged. We acknowledge National Institutes of Health (GM061555 and GM139064) for partial support. Minnesota Supercomputing Institute's support to V.N. is greatly appreciated. This research was supported in party by Lilly Endowment, Inc., through its support for Indiana University Pervasive Technology Institute, and in part by the Indiana METACyt Initiative. The Indiana MTACyt Initiative at IU was also supported in part by Lilly Endowment, Inc.

Notes and references

1 N. G. Connelly, J. A. McCleverty and C. J. Winscom, *Nature*, 1967, **216**, 999–1000.
2 R. Eisenberg, *Coord. Chem. Rev.*, 2011, **255**, 825–836.
3 R. Eisenberg and H. B. Gray, *Inorg. Chem.*, 2011, **50**, 9741–9751.
4 P. J. Chirik, *Inorg. Chem.*, 2011, **50**, 9737–9740.
5 W. Kaim, *Inorg. Chem.*, 2011, **50**, 9752–9765.
6 C. G. Pierpont, *Inorg. Chem.*, 2011, **50**, 9766–9772.
7 C. C. Scarborough and K. Wieghardt, *Inorg. Chem.*, 2011, **50**, 9773–9793.
8 A. L. Balch, *J. Am. Chem. Soc.*, 1969, **91**, 6962–6967.
9 A. L. Balch, *Inorg. Chem.*, 1971, **10**, 388–391.
10 J. S. Miller and A. L. Balch, *Inorg. Chem.*, 1971, **10**, 276–281.
11 A. L. Balch, I. G. Dance and R. H. Holm, *J. Am. Chem. Soc.*, 1968, **90**, 1139–1145.
12 A. Begum and S. Sarkar, *Eur. J. Inorg. Chem.*, 2012, **2012**, 40–43.
13 T. Birchall, *Can. J. Chem.*, 1969, **47**, 4563–4565.
14 T. Birchall and N. N. Greenwood, *J. Chem. Soc. A*, 1969, 286–291, DOI: 10.1039/j19690000286.
15 H. Jacobsen and J. P. Donahue, *Inorg. Chem.*, 2008, **47**, 10037–10045.
16 U. Jayarathne, K. Williams, V. M. Kasyanenko, J. T. Mague, I. V. Rubtsov and J. P. Donahue, *Polyhedron*, 2012, **31**, 98–103.
17 C. J. Jones, J. A. McLeverty and D. G. Orchard, *J. Chem. Soc., Dalton Trans.*, 1972, 1109–1114.
18 J. A. McCleverty, N. M. Atherton, N. G. Connelly and C. J. Winscom, *J. Chem. Soc. A*, 1969, 2242–2257, DOI: 10.1039/j19690002242.
19 J. A. McCleverty and T. A. James, *J. Chem. Soc. A*, 1970, 3318–3321.
20 J. A. McCleverty and D. G. Orchard, *J. Chem. Soc. A*, 1971, 3784–3789, DOI: 10.1039/j19710003784.
21 J. A. McCleverty and D. G. Orchard, *J. Chem. Soc. A*, 1971, 626–631, DOI: 10.1039/j19710000626.
22 S. Sproules and K. Wieghardt, *Coord. Chem. Rev.*, 2010, **254**, 1358–1382.
23 J. Stach, W. Dietzsch and R. Kirmse, *Z. Chem.*, 1979, **19**, 73–75.
24 E. J. Wharton and J. A. McCleverty, *J. Chem. Soc. A*, 1969, 2258–2266, DOI: 10.1039/j19690002258.
25 R. M. Buchanan and C. G. Pierpont, *J. Am. Chem. Soc.*, 1980, **102**, 4951–4957.
26 U. T. Mueller-Westerhoff, B. Vance and D. I. Yoon, *Tetrahedron*, 1991, **47**, 909.
27 C. G. Pierpont and R. M. Buchanan, *Coord. Chem. Rev.*, 1981, **38**, 45–87.
28 O. Sato, J. Tao and Y.-Z. Zhang, *Angew. Chem., Int. Ed.*, 2007, **46**, 2152–2187.
29 A. Davison, N. Edelstein, R. H. Holm and A. H. Maki, *J. Am. Chem. Soc.*, 1964, **86**, 2799–2805.
30 R. Eisenberg, E. I. Stiefel, R. C. Rosenberg and H. B. Gray, *J. Am. Chem. Soc.*, 1966, **88**, 2874–2876.
31 W. E. Broderick, E. M. McGhee, M. R. Godfrey, B. M. Hoffman and J. A. Ibers, *Inorg. Chem.*, 1989, **28**, 2902–2914.
32 E. I. Stiefel, R. Eisenberg, R. C. Rosenberg and H. B. Gray, *J. Am. Chem. Soc.*, 1966, **88**, 2956–2966.
33 C. R. Groom, I. J. Bruno, M. P. Lightfoot and S. C. Ward, *Acta Crystallogr.*, 2016, 171–179, DOI: 10.1107/S2052520616003954.
34 A. Sequeira and I. Bernal, *J. Cryst. Mol. Struct.*, 1973, **3**, 157–169.
35 C. Milsmann, S. Sproules, E. Bill, T. Weyhermueller, S. D. George and K. Wieghardt, *Chem. - Eur. J.*, 2010, **16**, 3628–3645, S3628/3621-S3628/3620.
36 S. P. Best, R. J. H. Clark, R. C. S. McQueen and J. R. Walton, *Inorg. Chem.*, 1988, **27**, 884–890.
37 L. Pilia, D. Espa, G. Concas, F. Congiu, L. Marchio, M. Laura Mercuri, A. Serpe and P. Deplano, *New J. Chem.*, 2015, **39**, 4716–4725.
38 S. C. Ratvasky, B. Mogesa, M. J. van Stipdonk and P. Basu, *Polyhedron*, 2016, **114**, 370–377.
39 K. J. Colston, S. A. Dille, B. Mogesa, A. V. Astashkin, J. A. Brant, M. Zeller and P. Basu, *Eur. J. Inorg. Chem.*, 2019, **2019**, 4939–4948.
40 B. Mogesa, E. Perera, H. M. Rhoda, J. K. Gibson, J. Oomens, G. Berden, M. J. van Stipdonk, V. N. Nemykin and P. Basu, *Inorg. Chem.*, 2015, **54**, 7703–7716.
41 R. P. Mtei, E. Perera, B. Mogesa, B. Stein, P. Basu and M. L. Kirk, *Eur. J. Inorg. Chem.*, 2011, **2011**, 5467–5470.
42 V. N. Nemykin, J. G. Olsen, E. Perera and P. Basu, *Inorg. Chem.*, 2006, **45**, 3557–3568.
43 E. Perera and P. Basu, *Dalton Trans.*, 2009, 5023–5028, DOI: 10.1039/b904113c.
44 J. Yang, B. Mogesa, P. Basu and M. L. Kirk, *Inorg. Chem.*, 2016, **55**, 785–793.
45 R. Isaksson, T. Liljefors and J. Sandstroem, *J. Chem. Res., Synop.*, 1981, **2**, 43.

46 G. M. Sheldrick, *SADABS Version 2.03*. University of Gottingen, Germany, 2002.
47 G. M. Sehldrick, *Acta Crystallogr., Sect. A: Found. Crystallogr.*, 2008, **64**, 112–122.
48 G. M. Sheldrick, *Acta Crystallogr., Sect. C: Cryst. Struct. Commun.*, 2015, **71**, 3–8.
49 C. B. Hubschle, G. M. Sheldrick and B. Dittrich, *J. Appl. Crystallogr.*, 2011, **44**, 1281–1284.
50 M. J. Frisch*et al.*, *Guassian09*, 2009.
51 A. L. Tenderholt, *QMForge2.4,* 2013.
52 F. A. Walker, *Coord. Chem. Rev.*, 1999, **185–186**, 471–534.
53 F. A. Walker, *Chem. Rev.*, 2004, **104**, 589–615.
54 F. A. Walker, *NMR and EPR Spectroscopy of Paramagnetic Metalloporphyrins and Heme Proteins*, World Scientific Publishing Co. Pte. Ltd, 2010.
55 J. D. Satterlee, *Concepts Magn. Reson.*, 1990, **2**, 69–79.
56 P. Basu, N. V. Shokhirev, J. H. Enemark and F. A. Walker, *J. Am. Chem. Soc.*, 1995, **117**, 9042.
57 G. R. Lewis and I. Dance, *Dalton Trans.*, 2000, 3176–3185, DOI: 10.1039/B000093K.
58 S. Sproules, *Prog. Inorg. Chem.*, 2014, **58**, 1–144.
59 P. Basu, K. J. Colston and B. Mogesa, *Coord. Chem. Rev.*, 2020, **409**, 213211.
60 K. N. Raymond, S. S. Isied, L. D. Brown, F. R. Fronczek and J. H. Nibert, *J. Am. Chem. Soc.*, 1976, **98**, 1767–1774.
61 A. S. Attia, B. J. Conklin, C. W. Lange and C. G. Pierpont, *Inorg. Chem.*, 1996, **35**, 1033–1038.
62 S. R. Boone, G. H. Purser, H. R. Chang, M. D. Lowery, D. N. Hendrickson and C. G. Pierpont, *J. Am. Chem. Soc.*, 1989, **111**, 2292.
63 L. Pilia, F. Artizzu, D. Espa, L. Marchio, M. L. Mercuri, A. Serpe and P. Deplano, *Dalton Trans.*, 2010, **39**, 8139–8142.
64 S. Sproules and K. Wieghardt, *Coord. Chem. Rev.*, 2011, **255**, 837–860.
65 F. Bigoli, P. Deplano, M. L. Mercuri, M. A. Pellinghelli, L. Pilia, G. Pintus, A. Serpe and E. F. Trogu, *Inorg. Chem.*, 2002, **41**, 5241–5248.
66 F. Bigoli, C.-T. Chen, W.-C. Wu, P. Deplano, M. L. Mercuri, M. A. Pellinghelli, L. Pilia, G. Pintus, A. Serpe and E. F. Trogu, *Chem. Commun.*, 2001, 2246–2247, DOI: 10.1039/b106064n.
67 E. A. M. Geary, L. J. Yellowlees, S. Parsons, L. Pilia, A. Serpe, M. L. Mercuri, P. Deplano, S. J. Clark and N. Robertson, *Dalton Trans.*, 2007, 5453–5459, DOI: 10.1039/b712243h.
68 R. Siebenlist, H.-W. Fruhauf, H. Kooijman, N. Veldman, A. L. Spek, K. Goubitz and J. Fraanje, *Inorg. Chim. Acta*, 2002, **327**, 66–89.